Automatic Detection of Caries in Dental X-Ray Images

JIHAD DABA, TONY ISSA, MOUSTAPHA EL HASSAN, ALI CHRAKIE
Department of Electrical Engineering,
University of Balamand,
Koura,
LEBANON

Abstract: - This paper presents a computer-aided pipeline for automatic caries detection in periapical dental radiographs that combines image processing with a bounded-speed level-set evolution. After denoising and contrast cleanup, Otsu thresholding, and morphological opening/closing, remove spurious structures. An integral projection isolates individual teeth, enabling a Morphological Region-Based Initial Contour (MRBIC) to seed a level-set segmentation driven by a normalized Signed Force Function (SFF). The SFF re-estimates inside/outside means at each iteration to self-calibrate to local intensity statistics, while motion filtering regularizes the evolving front; restricting evolution to a per-tooth window improves robustness near restorations and gaps. The scheme is CFL-stable, has linear per-iteration complexity in the active window, and reduces leakage and false edges compared with baseline methods. Using expert dentist annotations as ground truth, the system was evaluated on 120 periapical radiographs, achieving 90% tooth-level segmentation accuracy and 90% caries detection accuracy. These results indicate the scheme supports dentists with fast, reliable second-opinion screening.

Key-Words: - Dental X-ray images, detection, OTSU thresholding, segmentation.

Received: April 12, 2025. Revised: July 2, 2025. Accepted: August 11, 2025. Published: January 21, 2026.

1 Introduction

Detection of dental caries is essential for diagnosing and treating dental diseases, one of the most common diseases affecting many people worldwide. Doctors can detect the problem by visually inspecting an X-ray image of teeth. This method is very effective in detecting caries and best solves the problem. We will develop a diagnostic software tool to find out the infected area of the tooth, which will help make the doctors' job much easier and quicker. It allows more doctors without overworking them. The developed tool will provide a second opinion to assist the dentist, who ultimately makes the final diagnosis, to ensure the best patient care. In this work, we have developed a system for analyzing dental X-ray images using the most updated image processing techniques. We enhance the X-ray images for better quality and segment the infected regions of the teeth. We will have expert dentists label images of teeth against which to evaluate the accuracy of our system. The proposed method is very accurate and has promising results.

2 Problem Formulation

The early detection of dental caries is crucial for the diagnosis and treatment planning of dental conditions that affect a large population worldwide. For this purpose, dental X-rays are a valuable imaging tool that can provide dentists with a comprehensive evaluation of the teeth and gums, aiding in diagnosis and prevention, [1], [2]. Visual inspection alone has a low sensitivity rate, making X-rays an essential component of dental Imaging and diagnosis procedures, [3]. Many studies have focused on developing algorithms for measuring tooth decay and detecting caries, [4]. Image segmentation, a critical step in most medical image analysis applications, has been extensively studied in dental radiography, [5]. Researchers have proposed several approaches for tooth segmentation, including semi-automatic contour extraction using Bayes' rule and integral projection, [4], a three-step segmentation process involving picture enhancement, region of interest localization, and teeth segmentation, [6], as well as automated methods based on iterative and adaptive thresholding, [7]. Researchers have also proposed swarm-intelligence-based strategies and cellular-automata models for segmenting dental radiographs, [5]. Researchers have used mathematical morphology techniques to improve segmentation accuracy and suggested coupled level set functions for semi-automatic lesion identification, [2], [8]. Researchers have applied local singularity analysis

to dental picture segmentation, using Otsu thresholding and snake boundary tracking for tooth delineation, [7]. Various methods for individual tooth segmentation from CT images have been proposed, including the coupled variational level set method, [3]. Analyzing dental photos remains a challenging task compared to other medical imaging techniques. The obstacles comprise remnants from the medical process, obstructed molars, diverse dental anomalies, and spaces caused by absent teeth. Due to these obstacles, an appropriate approach for segmenting dental images continues to be complicated.

3 Problem Solution

This paper proposes a novel segmentation method and detection technique that improves the accuracy and reliability of the caries detection system. Figure 1 depicts the proposed framework, divided into three main phases: preprocessed, segmentation, and analysis. Two main stages conclude the segmentation phase: initial contour generation and level set segmentation.

Fig. 1: Framework of the segmentation and detection paradigm
Source: Created by the authors

3.1 Preprocessed

The dental X-ray image has noise, brightness, unwanted contrast, and unwanted details. For this reason, the Otsu method, [9], [10], detects the best threshold to remove undesired objects from the image.

Fig. 2: RGB images (a, b, c, d)
Source: Created by the authors

3.1.1 Data Collection

Acquiring the image is the first step in any image processing technique. A computer algorithm enhances the image and extracts valuable information.

3.1.2 Image Input

The system usually codes the acquired image in the RGB color space because it adheres to the jpg or jpeg standards (Figure 2).

3.2 Morphological Operations

Morphological techniques consist of a group of operations for image processing methods that change the form and construction in binary images; very often, thresholding connects them to enhance image segmentation results, for example, the detection of dental caries. In this step of the search-out analysis, the aim has been to determine how connected components based on the line possessions (area and measure) are, so avoidable objects have been removed. After thresholding, the system must eliminate a few remaining domains in the representations. The morphological open binary image technique would destroy all connected elements (objects) with predefined, hardly any specific pixels, and create another binary image. Definitely, small regions containing inferior pixels are certainly not a tooth field, and that may be the wax area or a few buzzes on radiograph concepts.

3.2.1 Opening

An opening is an erosion followed by a dilation with the same structuring element as in (1):

$$A \circ B = (A \ominus B) \oplus B \quad (1)$$

We note that the erosion locates all positions where the structuring element fits within the image but only marks those positions at the element's origin. A dilation after an erosion will fill the whole structuring element at the locations it fits within the object. Hence, an opening can capture all the possible translations of the structuring element that fit within the object. Openings are suitable for removing small objects, projections of objects, and connections between objects.

3.2.2 Closing

Closing works oppositely from the opening as in (2):

$$A \bullet B = (A \oplus B) \circ B \quad (2)$$

Opening deletes all the pixels where the structuring element cannot fit inside the image's foreground, while closing masks all those places where the

structuring element does not fit in the image's background. Note that duality does not imply involution: the result of a closing applied after an opening is not equal to the original image.

3.3 Integral Projection

Projection integrals are one of the most resorted-to means of analyzing and extracting information from an image. This technique can also quickly unravel one-dimensional feature edges and lines, constituting images' essential low-level interest features. It involves computing an integral image intensity along some particular axis in an image projection onto a one-dimensional histogram output.

Researchers have applied the technique of integral projection in various tasks related to image analysis, such as line and edge detection, measurement of angles and distances, and image segmentation by dividing images into regions of interest. It effectively processes images where the objects under observation align in a particular direction; for example, it handles teeth in dental radiography, which are usually vertically oriented.

If necessary, this script loads an image and preprocesses it to make the integral projection. The script then prompts the user to select a line or edge profile by inputting the starting point and orientation. Accordingly, the script integrates the image intensities along the selected profile in the axis direction to produce a one-dimensional array of values, which it then plots as a histogram showing the distribution of image intensities across the profile the user selects. With the generated histogram, the user can acquire information concerning those features of the image that are of interest.

We will use the integral projection method to separate each region of teeth. Let g(i, j) be the obtained m×n binary image from the thresholding step. The vertical integral projection method gives the position of the lines that separate each tooth from its neighbor, as in (3):

$$V(j) = \sum_{i=1}^{n} g(i,j). \quad (3)$$

3.4 Segmentation

The segmentation process aims to make work easier by converting the image to greyscale and then binarizing the image using a thresholding technique (Shuo et al., 2007; Xu, Yezzi Jr, & Prince, 2000; Malladi, Sethian, & Vemuri, 1995; Deng & Tsui, 2002; Nilsson & Heyden, 2002). In this work, the thresholding technique uses the Otsu method. The segmentation process is an essential step in every medical image analysis application. In this research, we have improved the accuracy and dependability of the caries detection system by using a new segmentation approach and detection technique. The three key aspects of the suggested framework are preprocessing, segmentation, and analysis.

3.4.1 Grey Scaling

The most commonly used images of type jpg and jpeg consist of RGB colors, [1]. We convert the RGB images to gray images by averaging the red, blue, and green values to determine the intensity of the grayscale image using the following equation (4):

$$Grayscale = \frac{R + G + B}{3} \quad (4)$$

R is the red pixel value, G is the green pixel value, and B is the blue pixel value.

3.4.2 Binarization

After grayscaling the image, we do Binarization (Figure 3), which transforms the grey image into a binary image. The binary image comprises two-pixel values, 1 or 0. Binary images enhance efficiency and reduce the processing load. Researchers may get binary images through Global Binarization and adaptive Binarization. Global Binarization comprises one threshold value for all images, whereas adaptive Binarization comprises changing threshold values for each pixel.

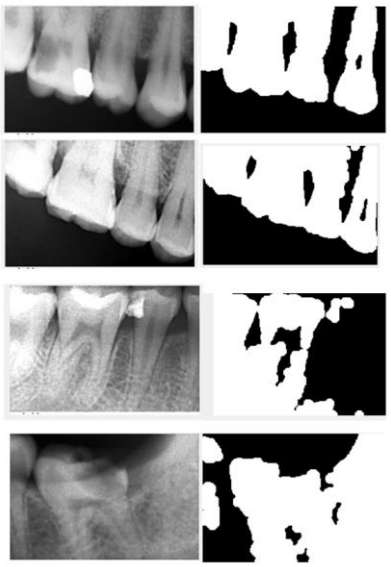

Fig. 3: Binarization (a, b, c, d)
Source: Created by the authors

3.4.3 Initial Contour and Level Segmentation

Segmentation is composed of 2 parts: initial contour generation and level set segmentation. The area of the surface where the contour level is zero, or the zero-level set, may be referred to as the

segmentation border. Let's stand for the implicit surface in the following way, as in (5):

$$\phi(x,t) = \pm d. \quad (5)$$

where x is a position in our domain (the image), t is time, and d is the distance or gap between position x and the zero-level. The sign in front of d is positive if x is outside the zero-level set. Otherwise, the sign is negative, [11]. The polarity of d affirms whether or not x lies outside the zero-level set.

Despite its benefits, the level-set approach still needs a few essential parameter values to be decided upon beforehand; for example, the starting contour point and the signed force function are among the parameters, [12]. The suggested methodology addresses the initial contour generation and the level set method's fundamental problems, enhancing the level set method's accuracy and robustness for segmenting dental images.

Fig. 4: The morphological region-based contour using algorithm 1
Source: Created by the authors

We implement the proposed Morphological Region-Based Initial Contour (MRBIC), [10], in Algorithm 1, which consists of 4 steps (Malladi, Sethian, & Vemuri, 1995):
Step 1. Input original image
Step 2. Binarization (using determined threshold values)
Step 3. For each labeled area < PPV (predefined pixel value), remove undesired objects
Step 4. Initial contour (IC) map (white square) (Figure 4)
Figure 4 shows the results of the MRBIC implemented in Algorithm 1.

The level set function is set to binary to simplify it, and then a motion filter is used to regularize it. The motion filter can smooth the level set function, making the valuation more stable. The Signed Force Function (SFF) function explained in [13], has a value range of [-1, 1]. It controls the signs of the forces inside and outside the ROI so that the contour shrinks when it is outside the object or expands when it is inside the object.

The level set method's signed force function (SFF) is critical. Below, we detail the proposed algorithm for the SFF function.
Step 1: Determine the Signed Force Function.

$$\mathrm{SFF}\big(I(\mathrm{x})\big) = \frac{I(x) - \frac{c_1+c_2}{2}}{\max(|I(x) - \frac{c_1+c_2}{2}|)}, x \in \Omega \quad (6)$$

$$\varphi(x,y,0) = \begin{Bmatrix} -d(x,y,\gamma) \ if \ (x,y) \ is \ inside \ the \ front \\ d(x,y,\gamma) \ if \ (x,y) \ is \ outside \ the \ front \end{Bmatrix} \quad (7)$$

Step 2. Compute c1(φ) and c2(φ) of Eq. (6).

$$c_1(\varphi) = \frac{\int_\Omega I(x).H(\varphi)dx}{\int_\Omega H(\varphi)dx} \quad (8)$$

$$c_2(\varphi) = \frac{\int_\Omega I(x).(1-H(\varphi))dx}{\int_\Omega (1-H(\varphi))dx} \quad (9)$$

Step 3. Evolve the level set function according to Eq. (10)

$$\frac{d\varphi}{dt}\mathrm{SFF}\big(I(x)\big).|\nabla\varphi|, x \in \Omega_0 \quad (10)$$

In the proposed framework, Ω0 represents a subset within the image domain Ω, and ∂Ω0 denotes the boundary of Ω0.
Step 4. Let φ = 1 if φ > 0; otherwise, φ = −1. This step has the local segmentation property. It is necessary to segment the desired objects selectively; otherwise, it is unnecessary.

Step 5. Regularize the level set function with motion filter, i.e., φ = φ ∗ Mσ for appropriately chosen scaling parameters M and σ.
Step 6. Check whether the evaluation of the level set function has converged. If not, return to Step 2.
Figure 5 shows the morphological region-based contour using the proposed methodology. Compared to Figure 4, it is clear that the proposed method eliminates erroneous edges in the image and shows more accurate results. Achieving more accurate results requires additional computational time,

which is not critical if the photos are not analyzed immediately in real time.

Fig. 5: The morphological region-based contour using the proposed methodology
Source: Created by the authors

The appendix at the end of this work provides formal derivations of Eqs. (6) and (10) for the segmentation model employed in this paper.

3.5 Signed Force Function in Noisy Dental X- Rays

This section discusses why this SFF-driven evolution remains accurate and stable in noisy dental radiographs.

Dental periapical radiographs present low contrast, heterogeneous illumination, metallic restorations, overlapping structures, and film/sensor artifacts. The SFF scheme ensures accurate evolution in noisy dental X-rays because it is tailored to the following six conditions.

3.5.1 Statistical Centering at the Evolving Interface

The decision boundary is the midpoint m, recomputed from current inside/outside assignments via Eq. (B). This makes the force self-calibrating to the actual tooth/background brightness in the current image (and even in a local subdomain Ω_0 if desired). Regions that are dimmer/brighter in one patient (or one tooth) do not break the method–the threshold tracks them. This is much more robust than a fixed global threshold in the presence of variable exposure and scatter.

3.5.2 Sign-correct Expansion/Shrinkage

Because SFF $\propto I - m$, pixels with $I > m$ push the front outward (+), and pixels with $I < m$ pull it inward (-), ensuring that the contour moves in the correct direction even when edge gradients are weak (common in carious regions). The algebraic identity (D) shows this is exactly the sign of the classical Chan–Vese data force, so SFF preserves proven region-based behavior while simplifying scaling.

3.5.3 Contrast Normalization to [-1, 1]

Dividing by $\max|I - m|$ yields a bounded speed. In noisy/low-dynamic-range radiographs, this prevents overshooting (where small noise spikes could otherwise cause very large updates) and gives a stable time step across images. It also reduces sensitivity to sensor gain differences, post-processing variations, or JPEG compression.

3.5.4 Local Evolution on Per-Tooth Window Ω_0

Using integral projection to isolate each tooth, then evolving only on Ω_0 , sharply reduces the class imbalance and distractor influence (neighboring teeth, bone patterns, metallic fillings). The statistics c_1, c_2 become localized to the tooth of interest, which improves discrimination at fuzzy enamel–dentin or lesion boundaries.

3.5.5 Regularization by Motion Filtering (Implicit Curvature)

Smoothing ϕ after each update damps jaggedness introduced by noise, emulating the effect of a curvature term (short-curve bias) without explicitly changing the PDE. This prevents the front from latching onto spurious speckles or trabecular noise while still allowing it to pass through weak edges (important where caries blur edges).

3.5.6 Robust Initialization via MRBIC

The morphological region-based initial contour (MRBIC), following thresholding and opening/closing, removes tiny artifacts (cement lines, sensor dust) and ensures the zero-level set begins near the correct basin of attraction. Good ICs are essential in low-SNR images; otherwise, any level-set scheme can converge to wrong structures.

3.6 Stability of the Two Auxiliary Steps

This section presents a stability analysis for the proposed SFF-driven level-set segmentation.

3.6.1 CFL Condition (discrete L^∞ stability)

Since $|F| \leq 1$ by construction (SFF is normalized to [-1, 1]), the standard Courant-Friedrichs-Lewy

(CFL) condition for explicit Godunov schemes of $\varphi_t + H(\nabla\varphi) = 0$ with $H(p) = -F\|p\|$ reads

$$\Delta t \leq \frac{\square}{max_{\Omega_0}|F|} \leq \square. \quad (11)$$

3.6.2 Stability of the Two Auxiliary Steps

With $\Delta t \leq \square$, the explicit SFF-advection step is L^∞-stable and the subsequent binarization and motion-filter steps are non-expansive as elaborated below:

1. Binarization $\varphi \leftarrow sign(\varphi)$ maps into $\{\pm 1\}$ and is trivially L^∞-non-expansive; it cannot blow up amplitudes. This step is part of the "local segmentation property".
2. Motion filter $\varphi \leftarrow \varphi * M_\sigma$ with a nonnegative kernel of unit mass is a contraction in both L^1 and L^∞ norms (Young's inequality). Hence, the smoothing step is also stable and damps high-frequency noise.

Therefore, the full outer iteration is stable.

3.7 Convergence of the Partial Differential Equation Discretization (Viscosity-Solution Sense)

This section presents a convergence analysis for the proposed SFF-driven level-set segmentation. For a fixed field $F(x)$ that is bounded and Lipschitz, a monotone, consistent, and stable Godunov scheme converges to the unique viscosity solution as $\Delta t, \square \to 0$ (classical Barles-Souganidis/Osher-Sethian theory). In the employed segmentation algorithm, F is not fixed but re-estimated from φ via $c_1(\varphi)$, $c_2(\varphi)$ after each outer iteration using Eqs. (8) and (9).

If one iteration is regarded as:

1. freeze $F^n = SFF\big(I; c_1(\varphi^n), c_2(\varphi^n)\big)$;
2. advance φ by the monotone scheme for time Δt;
3. binarize and smooth φ;

then each inner step converges as $\square, \Delta t \to 0$. The outer space $\{\varphi^n, c_1^n, c_2^n\}$ is bounded by the above stability plus bounded intensities, and every limit point satisfies the stationarity condition $F(x) = SFF(I(x); c_1, c_2) = 0$ on the zero level set Γ which is equivalent to $I(x) = (c_1 + c_2)/2$ on Γ (or the trivial case $c_1 = c_2$). This characterizes fixed points of Eq. (10).

3.8 Computational Complexity of the SFF-driven Level-set Segmentation

This section presents a complexity analysis for the proposed SFF-driven level-set segmentation and offers a comparison with other schemes.

Let $N = |\Omega_0|$ be the number of pixels in the active tooth window. Per outer iteration:

1. Compute c_1, c_2: two integrals + two counts over $\Omega_0 \Rightarrow \mathrm{O}(N)$.
2. Compute m and $max|I - m|$: one pass $\Rightarrow \mathrm{O}(N)$.
3. One explicit SFF step with Godunov differences: constant work per pixel $\Rightarrow \mathrm{O}(N)$.
4. Binarization: $\mathrm{O}(N)$.
5. Motion filter M_σ: separable $k \times k$ kernel cost $\mathrm{O}(kN)$ with small fixed $k \Rightarrow \mathrm{O}(N)$.

Iteration cost. The per-iteration cost is linear in N with a small constant; memory is also $\mathrm{O}(N)$ (store I, ϕ, and a few temporaries).

Iteration count. Because $|F| \leq 1$, the choice of $\Delta t \approx \square$ (CFL-tight) is feasible, which reduces the number of iterations relative to curvature-dominant schemes that require $\Delta t = \mathrm{O}\left(h^2\right)$.

The computational cost and stability of the proposed SFF-driven level-set segmentation are summarized and compared with common alternatives in Table 1 (Appendix).

4 Conclusion

The presented work described a precise segmentation technique in the periapical dental radiographs. The approach had segmented 65 teeth from 32 images that contained 72 teeth. A thresholding method and a morphologically opening binary image technique are applied to remove the unnecessary objects from the image. An integral projection technique locates each tooth's horizontal and vertical straight lines in the image. The level set method also enabled us to extract dental photos of each tooth subsequently and segment the exact critical region of the teeth within it. The findings for the proposed approach should be accurate and work well.

Future work should improve the method by considering variations in teeth and missing tooth spaces, which can pose challenges in radiograph images noting that deep learning systems tend to produce a high misdetection rate at the tooth boundaries but much higher detection rates inside

the tooth fabric, future work should focus on improving the segmentation scheme by making it more adaptive, [14], [15], [16],, and combining it with a deep neural network to achieve excellent results both inside and on the edges of teeth.

Future work will also focus on making the SFF-level-set pipeline more adaptive, robust, and deployable as per the flowing proposed steps: (i) introduce boundary-aware statistics (local c_1, c_2) and light shape/topology priors to sharpen edges without over-constraining anatomy; (ii) explicitly model gaps/missing teeth via gap likelihoods and motion attenuation to prevent leakage across edentulous spaces; (iii) improve noise resilience through robust (Huber/trimmed) region statistics and bias-field correction; (iv) develop hybrid learning variants, convolutional neural network (CNN) cues fused with the bounded-speed geometric update, and unrolled SFF iterations trained end-to-end to preserve classical stability while leveraging data; (v) strengthen initialization and automatic selection of Ω_0 with learned seeds and quality-checked projection peaks; (vi) add adaptive time-stepping, energy/statistic monitors, and re-initialization triggers for provable, practical convergence; (vii) extend to multi-tooth instance segmentation with non-overlap constraints and confidence scoring; (viii) run broader clinical validation (Dice/Hausdorff, reader studies, modality generalization); and (ix) optimize for chair-side use via separable filters, GPU tiling, and mixed-precision to keep complexity linear and latency low.

Declaration of Generative AI and AI-assisted Technologies in the Writing Process

The authors wrote, reviewed and edited the content as needed and verifies that none utilized artificial intelligence (AI) tools were used. The authors take full responsibility for the content of the publication.

References:

[1] Sabbaghi, S., Aldeen, M., Garnavi, R., Varigos, G., Doliantis, C., & Nicolopoulos, J. (2015). Automated colour identification in melanocytic lesions. *37th Annual International Conference of the IEEE on Electrical and Computer Engineering*, 3021–3024. IEEE. doi: 10.1109/EMBC.2015.7319028.

[2] Eyad Haj, S., Nassar, D.E.M., & Ammar, H.H. (2006). Image segmentation for automated dental identification. *Electronic Imaging*, 60640X–60640X. doi: 10.1117/12.650757.

[3] Gao, H., & Chae, O. (2010). Individual tooth segmentation from CT images using level set method with shape and intensity prior. *Pattern Recognition*, 43(7), 2406–2417. doi: 10.1016/j.patcog.2010.01.010.

[4] Jain, A.K., & Chen, H. (2004). Matching of dental X-ray images for human identification. *Pattern Recognition*, 37(7), 1519–1532. doi: 10.1016/j.patcog.2003.12.016..

[5] Keshtkar, F., & Gueaieb, W. (2006). Segmentation of dental radiographs using a swarm intelligence approach. *Canadian Conference on Electrical and Computer Engineering*, 328–331. IEEE. https://doi.org/10.1109/CCECE.2006.277656.

[6] Kutsch, V.K. (2011). Caries detection. *Inside Dentistry*, AEGIS Communications, [Online]. https://insidedentistry.net/2011/08/caries-detection/ (Accessed Date: January 5, 2025).

[7] Lin, P., Huang, P., Huang, P., Hsu, H., & Chen, C. (2014). Teeth segmentation of dental periapical radiographs based on local singularity analysis. *Computer Methods and Programs in Biomedicine*, 113(2), 433–445. doi: 10.1016/j.cmpb.2013.10.015.

[8] Molteni, R. (1993). Direct digital dental X-ray imaging with Visualix/VIXA. *Oral Surgery, Oral Medicine, Oral Pathology*, 76(2), 235–243. doi: 10.1016/0030-4220(93)90211-L.

[9] Nomir, O., & Abdel-Mottaleb, M. (2007). Human identification from dental X-ray images based on the shape and appearance of the teeth. *IEEE Transactions on Information Forensics and Security*, 2(2), 188–197. doi: 10.1109/TIFS.2007.897245.

[10] Rad, A.E., Mohd Rahim, M.S., Kolivand, H., & Mat Amin, I.B. (2017). Morphological region-based initial contour algorithm for level set methods in image segmentation. *Multimedia Tools and Applications*, 76(2), 2185–2201. doi: 10.1007/s11042-015-3196-y.

[11] Deng, J., & Tsui, H.T. (2002). A fast level set method for segmentation of low contrast noisy biomedical images. *Pattern Recognition Letters*, 161(9), 1049–1055. doi: 10.1016/S0167-8655(01)00113-1.

[12] Nilsson, B., & Heyden, A. (2002). A fast algorithm for level set like active contours. *Pattern Recognition Letters*, 24(9–10), 1331–1337. doi: 10.1016/S0167-8655(02)00374-4.

[13] Xu, C., Yezzi Jr, A., & Prince, J. L. (2000). On the relationship between parametric and geometric active contours. *Conference on*

Record of the Thirty-Fourth Asilomar, 1, 483–489. IEEE. doi: 10.1109/ACSSC.2000.911003.

[14] Dubois, J. & Abdul-Latif O. (2005). Detection of Ultrasonic Images In the Presence of a Random Number of Scatterers: A Statistical Learning Approach. *International Enformatika Conference* (IEC), Prague, 326-329, [Online]. https://dblp.org/db/conf/wec/iec2005prague.html#DuboisA05c (Accessed Date: March 3, 2025).

[15] Dubois, J. (2002). Segmentation of speckled ultrasound images based on a statistical model. *EURASIP Proceedings of the 16th International Biosignal Conference*, 377–380.

[16] Bell, M. R., & Daba, J. (1994). Object discrimination and orientation determination in speckled images. *Optical Engineering*, 33(4), 1287–1303. doi: 10.1117/12.166933.

Contribution of Individual Authors to the Creation of a Scientific Article (Ghostwriting Policy)

Jihad Daba and Tony Issa conceptualized the research.
Jihad Daba and Tony Issa developed the methodology.
Jihad Daba formulated and analyzed all mathematical models.
Tony Issa simulated the proposed algorithm.
Jihad Daba and Moustapha El Hassan carried out the validation.
Tony Issa, Jihad Daba, Ali Chrakie, and Moustapha El Hassan conducted the formal analysis.
Jihad Daba and Moustapha El Hassan were responsible for the investigation.
Tony Issa and Ali Chrakie provided the necessary resources and managed data maintenance.
Jihad Daba, Moustapha El Hassan, and Ali Chrakie wrote the initial draft.
Jihad Daba, Moustapha El Hassan, and Ali Chrakie reviewed and edited the manuscript.
Jihad Daba, Moustapha El Hassan, and Ali Chrakie prepared the visualizations.
Jihad Daba was responsible for supervision.
Jihad Daba, Tony Issa, Moustapha El Hassan, and Ali Chrakie managed the project.

All authors have read and agreed to the published version of the manuscript.

Sources of Funding for Research Presented in a Scientific Article or Scientific Article Itself

The University of Balamand funded this study.

Conflict of Interest

The authors have no conflicts of interest to declare that are relevant to the content of this article.

Creative Commons Attribution License 4.0 (Attribution 4.0 International, CC BY 4.0)

This article is published under the terms of the Creative Commons Attribution License 4.0
https://creativecommons.org/licenses/by/4.0/deed.en_US

APPENDIX

Table 1. Comparison to Common Alternatives

Method	Per-iteration complexity	Stability time step	Comments
Proposed SFF-LS	$O(N)$	$\Delta t \le h$	No curvature term; bounded speed; local window Ω_0 improves constants.
Chan-Vese with curvature	$O(N)$	$\Delta t = O\left(h^2\right)$	Extra curvature evaluation and a stiffer time step increase iteration count.
Geodesic active contours (edge-based)	$O(N)$ plus gradient prefilter	$\Delta t \le h$ (advection) and curvature are often used	Requires precomputing.
s/t Graph-cut (binary)	$\approx O(N) - O(N\sqrt{N})$ depending on the graph and implementation	n/a	Often very fast in practice, but it needs graph construction; it's hard to localize to Ω_0 with the same flexibility.
CNN (e.g., U-Net inference)	$O(N)$ with a large constant (FLOPs/px)	n/a	Fast at inference on GPU, but requires training; less controllable at tooth borders (as noted in this paper).

Source: Created by the authors

Appendix A. Formal Derivations of the Employed Segmentation Scheme

This Appendix provides formal derivations that connect a region-based level-set energy to the specific "signed force function" (SFF) used in the dental X-ray pipeline of this work in section 3.4.3 and formulated in Eqs. (6) and (10).

A1. Region Energy

Let $I: \Omega \subset \square^2 \to \square$ be the gray-level image, $\varphi(x,t)$ a level-set function whose zero level $\Gamma(t) = \{x|\varphi(x,t) = 0\}$ is the evolving contour, and H_ε and $\delta_\varepsilon = H_\varepsilon'$ the regularized Heaviside and Dirac distributions, respectively. Inside/outside the contour is indicated by $H_\varepsilon(\varphi)$ and $1 - H_\varepsilon(\varphi)$.

Consider the standard region-based (Chan-Vese-type) energy without explicit curvature regularization (regularization is applied via smoothing of φ as per this work's method):

$$\xi(\varphi, c_1, c_2) = \int_\Omega \Big((I(x) - c_1)^2 H_\varepsilon(\varphi(x)) + (I(x) - c_2)^2 \big(1 - H_\varepsilon(\varphi(x))\big) \Big)\, dx. \quad \text{(A)}$$

Here c_1 and c_2 are region statistics (means) for "inside" and "outside".

Optimal c_1 and c_2. Minimizing ξ with respect to c_1 and c_2 (by setting partial derivatives to zero) gives

$$c_1(\varphi) = \frac{\int_\Omega I(x) H_\varepsilon(\varphi(x))\, dx}{\int_\Omega H_\varepsilon(\varphi(x))\, dx}, \quad \text{(B1)}$$

$$c_2(\varphi) = \frac{\int_\Omega I(x) \big(1 - H_\varepsilon(\varphi(x))\big)\, dx}{\int_\Omega \big(1 - H_\varepsilon(\varphi(x))\big)\, dx}, \quad \text{(B2)}$$

which are exactly the expressions implemented in this work's pipeline.

Gradient descent in ϕ. Taking the L^2 gradient flow in ϕ gives

$$\frac{\partial \varphi}{\partial t} = -\frac{\partial \xi}{\partial t} = -\delta_\varepsilon(\varphi)[(I - c_1)^2 - (I - c_2)^2]. \quad \text{(C)}$$

Algebraic manipulations of the bracketed term in Eq. (C) yield a crucial factorization:

$$(I - c_1)^2 - (I - c_2)^2 = (c_2 - c_1)\big(2I - (c_1 + c_2)\big) = 2(c_2 - c_1)(I - m),\ m \triangleq \frac{c_1 + c_2}{2}. \quad \text{(D)}$$

Hence, the sign of the data force is the sign of $I - m$: intensities above the midpoint m favor "inside", below favor "outside".

A2. Geometric Level-set Form and the Signed Force Function (SFF)

It is standard to recast the evolution as a geometric normal-speed motion:

$$\frac{\partial \varphi}{\partial t} = F(x)|\nabla \varphi|, \quad \text{(E)}$$

where F is the normal speed (positive expands the contour, negative shrinks it). Comparing Eqs. (C) and (D) with Eq. (E) shows that a data-driven speed proportional to the sign $(I - m)$ is natural.

This work's implementation turns into a bounded, contrast-normalized signed force

$$SFF(I(x))) = \frac{I(x)-m}{\max_{y\in\Omega}|I(y)-m|} \in [-1,1] \quad \text{(F)}$$

and uses

$$\frac{\partial\varphi}{\partial t} = SFF(I(x))|\nabla\varphi| \ \ on \ \ \Omega_0 \subseteq \Omega. \quad \text{(G)}$$

Equations (F) and (G) respectively match Eq. (6) and Eq. (10) in this work: The SFF is normalized, signed indicator relative to the current region statistics (c_1, c_2), and the evolution is geometric with speed F = SFF. The Ω_0 restriction enables selective/local evolution per tooth refinement.